Surface displacement of the Mw 7 Machaze earthquake (Mozambique): Complementary use of multiband InSAR and radar amplitude image correlation with elastic modelling.

Daniel Raucoules, B. Ristori, Marcello de Michele, P. Briole

Surface displacement of the M_w 7 Machaze earthquake (Mozambique): Complementary use of multiband InSAR and radar amplitude image correlation with elastic modelling.

Raucoules D. (1), Ristori B. (1), de Michele M. (1), Briole P. (2)

(1) BRGM 3 avenue Claude Guillemin 45060 Orléans cedex 2 France

Corresponding author: d.raucoules@brgm.fr

(2) ENS, Laboratoire de Géologie, 24 Rue Lhomond, 75005 Paris

Abstract

In this paper we investigate the surface displacement related to the 2006 Machaze earthquake using Synthetic Aperture Radar Interferometry (InSAR) and sub-pixel correlation (SPC) of radar amplitude images. We focus on surface displacement measurement during three stages of the seismic cycle. First, we examined the co-seismic stage, using an Advanced SAR (ASAR) sensor onboard the Envisat satellite. Then we investigated the post-seismic stage using the Phase Array L-band SAR sensor (PALSAR) onboard the ALOS satellite. Lastly, we focussed on the inter-seismic stage, prior to the earthquake by analysing the L-band JERS-1 SAR data. The high degree of signal decorrelation in the C-band co-seismic interferogram hinders a correct positioning of the surface rupture and correct phase unwrapping. The post-seismic L-band interferograms reveal a time-constant surface displacement, causing subsidence of the surface at a ~ 5 cm/yr rate. This phenomenon continued to affect the close rupture field for at least two years following the earthquake and intrinsically reveals a candidate seismogenic fault trace that we use as a proxy for an inversion against an elastic dislocation model. Prior to the earthquake, the JERS interferograms do not indicate any traces of pre-seismic slip on the sismogenic fault. Therefore, slip after the earthquake is post-seismic, and it was triggered by the Machaze earthquake. This feature represents a prominent post-seismic slip event rarely observed in such a geodynamic context.

1 Introduction

On February 22, 2006, a M_w 7.0 earthquake occurred in Machaze, Manica Province, Mozambique (Figure 1) affecting an area characterised by low-level historical seismicity. This earthquake inflicted little damage on property and individuals, mainly because of the typology and density of housing in the area (i.e. scattered villages with light-weight structures). During the 20th century, three earthquakes with magnitudes larger than 5.0 concerned this area: the first in 1951 and the two others in 1957. They were characterised by shallow slip at depths of less than 20 km (Fenton & Bommer, 2006). The fault system associated with these earthquakes can be related to the southern portion of the East African Rift and belongs to a divergent plate-boundary geodynamic context. The 2006 Machaze earthquake occurred at a depth of 12 km and produced a north-south oriented surface rupture about 30-40 km long with a co-seismic surface slip of up to 2 metres (Fenton & Bommer, 2006). The fault ruptured with a normal mechanism with a 70° west dipping fault plane. Fenton & Bommer (2006) stated that the surface rupture, although visible in the field, could not be followed along its entire length due to the danger posed by buried land mines in the area. Moreover, extensive liquefaction phenomena were associated to this event (Lopez-Querol et al., 2007).

In this paper, we called on remote-sensing satellite data to complement data acquired on the ground to help understand the Machaze earthquake. In particular, we used InSAR (e.g. Massonnet & Feigl, 1998) and SPC (e.g. Michel & Avouac, 2002) techniques along with Envisat-ASAR, JERS-1 and ALOS-PALSAR data to measure the ground surface displacement produced by the Machaze earthquake at different stages of the seismic cycle, i.e. before, during and after the earthquake. Then, we used the co-seismic displacement field to constrain the seismogenic fault geometry at depth by inverting the surface displacement field against a simple elastic dislocation model (Briole et al., 1986).

We proceeded as follow. First, we used the ALOS PALSAR data to produce a post-seismic interferogram revealing the position and surface geometry of the seismogenic fault (not observable on the co-seismic interferograms because of high deformation rates). Then we looked at the inter-seismic interferograms to detect possible creep or pre-seismic slip on this previously unmapped fault. Finally, we built a co-seismic interferogram and used the retrieved fault surface geometry parameters to constrain the fault's co-seismic slip and geometry at depth by means of an inversion procedure.

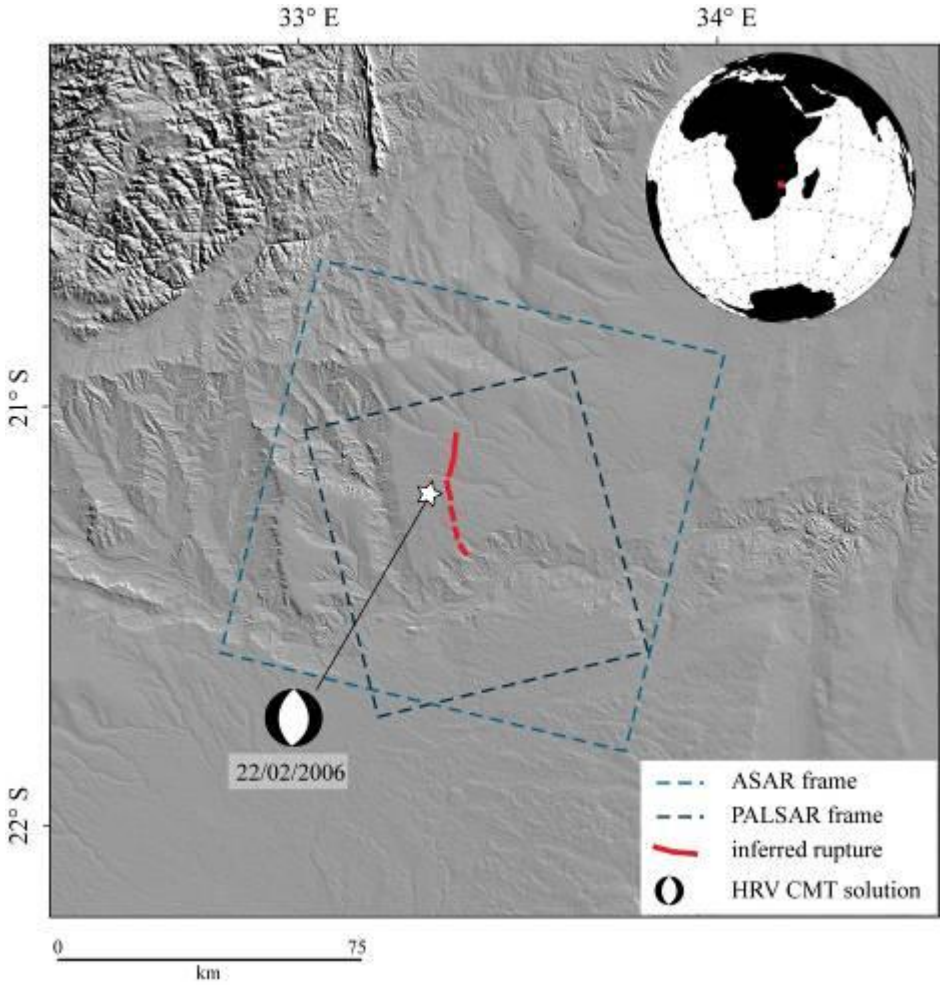

Figure 1 : Location of the Machaze Earthquake

2 Data

In this study, we made ~~a~~ complementary use of C and L band radar from different sensors. Due to the dense vegetation covering the terrain in the area of interest and the large size of surface deformation expected (~ metre), we decided to use ALOS-PALSAR and JERS-1 L-band radar data. Moreover, the measurements obtained from radar data at longer wavelengths (23 cm as opposed to 5.6 cm for C-band) would be less affected by fringe aliasing as there would be fewer fringes for given deformation values. Therefore, interferometric phases could be unwrapped over larger areas (e.g. Raucoules et al., 2007). Unfortunately, ALOS and JERS-1 data were not available during the co-seismic phase of the Machaze earthquake. We accordingly called on Envisat/ASAR C-band data to retrieve co-seismic surface displacement while using

ALOS-PALSAR and JERS-1 to investigate possible post-seismic and pre-seismic surface displacement respectively. In this study we used six PALSAR images (Dec. 2006- Dec. 2008, ascending mode), seven ASAR images (Nov. 2003, Feb. 2007, descending mode) and three JERS-1 images (Apr. 1993 – Oct. 1996, ascending mode). Tables 1 to 3 describe the characteristics of the PALSAR, ASAR and JERS-1 interferograms that we built using the GAMMA software (Wegmuller et al., 1998).

Table 1: Interferograms produced using ALOS PALSAR SAR images. Post-seismic period.

Interferogram	**Image1 (date)**	**Image2 (date)**	***Perpendicular baseline (m)***	***Time span (days)***
1	20061226	20070210	725	46
2	20061226	20071229	-881	368
3	20061226	20080213	-632	414
4	20061226	20080330	-1191	460
5	20061226	20081231	1512	736
6	20070210	20071229	-1607	322
7	20070210	20080213	-1357	368
8	20070210	20080330	-1916	414
9	20070210	20081231	787	690
10	20071229	20080213	249	46
12	20071229	20081231	2394	368
13	20080213	20080330	-558	46
14	20080213	20081231	2145	322
15	20080330	20081231	2704	276

Table 2: Interferograms produced using ASAR Envisat SAR images. Co-seismic period.

Interferograr	***Image1***	***Image2***	**Perpendicular baseline *(m)***	**Time span (days)**
1	20031109	20060507	720	910
2	20031109	20060611	230	945
3	20031109	20070211	432	1190
4	20040118	20060507	1114	840
5	20040118	20060611	623	875
6	20040118	20070211	826	1120
7	20040328	20060507	-131	770
8	20040328	20060611	-622	805
9	20040328	20070211	-420	1050
10	**20040606**	**20060507**	**-198**	**700**
11	20040606	20060611	-689	735
12	20040606	20070211	-486	980

Table 3: Interferograms produced using JER-1 SAR images. Pre-seismic period.

Interferogram	**Image1**	**Image2**	***Perpendicular baseline (m)***	Time span (days)
1	19930406	19950311	-68	704
2	19930406	19960820	110	1232
3	19950311	19960820	179	528

3 Data Processing

Post-seismic Slip

For each of the three observation periods, we apply different processing strategies.

- Hashimoto et al. (2007) detected and provided a preliminary estimate of the post-seismic deformation phenomenon based on a single ALOS/PALSAR pair prior to December 2006. Our objective here has therefore been to obtain a precise location of the displacement field and to derive the post-seismic displacement rate over a longer period. We further would be interested in ascertaining whether post seismic displacement is decelerating. In this perspective, we built a stack of 15 unwrapped interferograms according to the methodology proposed by Le Mouelic et al. (2005):

[eq 1]
$$V = \frac{\langle \Delta\Phi \rangle}{\langle \Delta T \rangle} \frac{\lambda/2}{2\pi}$$

Brackets in eq. 1 indicate the average value on the data set. $\Delta\Phi$ is the interferometric phase, ΔT is the time span associated with an interferogram and λ is the wavelength.

Under such conditions, averaging a series of interferograms reduces the relative importance of the atmospheric component of the interferometric phase as compared with the displacement signal. Considering the characteristics of the studied phenomenon (slow deformation with respect to the sensor wavelength) and the good coherence of the interferograms, unwrapping errors will be reduced and should not impact the velocity map.

Then, based on an optimization procedure, we estimated the velocity by linear regression (Gamma, 2008). The result of this procedure was observed to be equivalent to that obtained by averaging. However, the linear regression procedure allows an image to be achieved of the discrepancy with respect to the linear regression (standard deviation) which provides quality control for the velocity estimation (in particular including temporal fluctuation due to atmospheric effects), and useful information to identify possible non-linear-with-time slip evolution during the observation period. The process accordingly yields a displacement rate map and a map showing discrepancy with respect to linearity (Figures 2a, 2b).

Inter-seismic Slip

- Our objective for the pre-seismic period was to detect pre-seismic deformation. We therefore constructed interferograms covering long time spans and examined them near the location of the earthquake rupture. We should mention that the JERS-1 provides poor coverage for this study area (only three images acquired).

Co-seismic Slip

- In order to map the co-seismic surface displacement, we built 12 differential interferograms. After visual comparison of all the interferometric series produced (Table 2), we selected interferograms having the least noise. In view of the high displacement rate (tens of interferometric fringes), the atmospheric component of the interferometric phase is negligible with respect to the displacement component. The results are shown in Figure 4.

As direct unwrapping is not relevant (areas with major deformation are not amenable because of the high fringe rate), visible fringes were digitised manually in order to perform an inversion of a dislocation model (Okada, 1985; Briole, 1986). Considering such a model as a direct source of information about the phenomenon, we proposed to re-inject the inverted parameters so as to produce a simulated interferogram. Once the simulated interferogram was subtracted from the initial interferogram, we obtained a residual, which is easier to unwrap. The unwrapped residual was added to the simulated interferograms and provided an improved unwrapped differential interferogram (Section 5).

It should be stated that the global unwrapping method used by Gamma tends to underestimate phase gradient value where the residual image is noisy. The simulation can therefore help correct these errors. To simplify the principle behind the proposed method, where the phase is noisy, the final result will correspond to the model and where the initial interferogram signal is reliable, the result will correspond to the interferometric data. In a certain way, this procedure interpolates the interferogram on the noisy areas (and in particular in the near-field deformation area) by taking into account a physical model based on the far-field deformation obtained by InSAR and ancillary knowledge about the earthquake.

4 Results

Post-seismic Slip

Figure 2a shows the displacement map derived from PALSAR interferometry. The most prominent feature in the post-seismic displacement map is the constant-with-time subsidence affecting the area formerly ruptured. The RMSE to linearity (Figure 2b) shows no correlation between the position of the rupture and the discrepancy with respect to linearity. That suggests that surface displacement is characterised by a constant rate over the 2-year observation period. In fact, the deformation along the rupture appears as linear as on stable areas (where deformation is obviously linear), far from the rupture. We measured a post-seismic surface displacement up to 3.5 cm/year, assuming a mainly vertical displacement phenomenon consistent with a 70°-dip normal fault. This phenomenon affected the study area for at least two years after the earthquake. According to our observations, post-seismic displacement did not decrease with time, though this might be due to the relatively short window of observation. Assuming that the post-seismic displacement occurred on the initial seismic rupture location, we can clearly locate (and digitise) a candidate for the co-seismic surface rupture. At this stage of the processing, one might think that the seismogenic fault underwent pre-seismic slip or creeping. We subsequently assessed the pre-seismic displacement field in the near-fault field and tried to discriminate between post-seismic relaxations and a possible pre-seismic slip component, which in principle should affect the area before the event as well.

Another prominent feature in the post-seismic displacement map is a 5 cm/yr vertical displacement feature located NNW of Figure 2. At first sight, this phenomenon is difficult to correlate with the 2006 Machaze earthquake as it is located 10 km west of the main rupture. Although not addressed in detail here, this phenomenon certainly does merit further investigation.

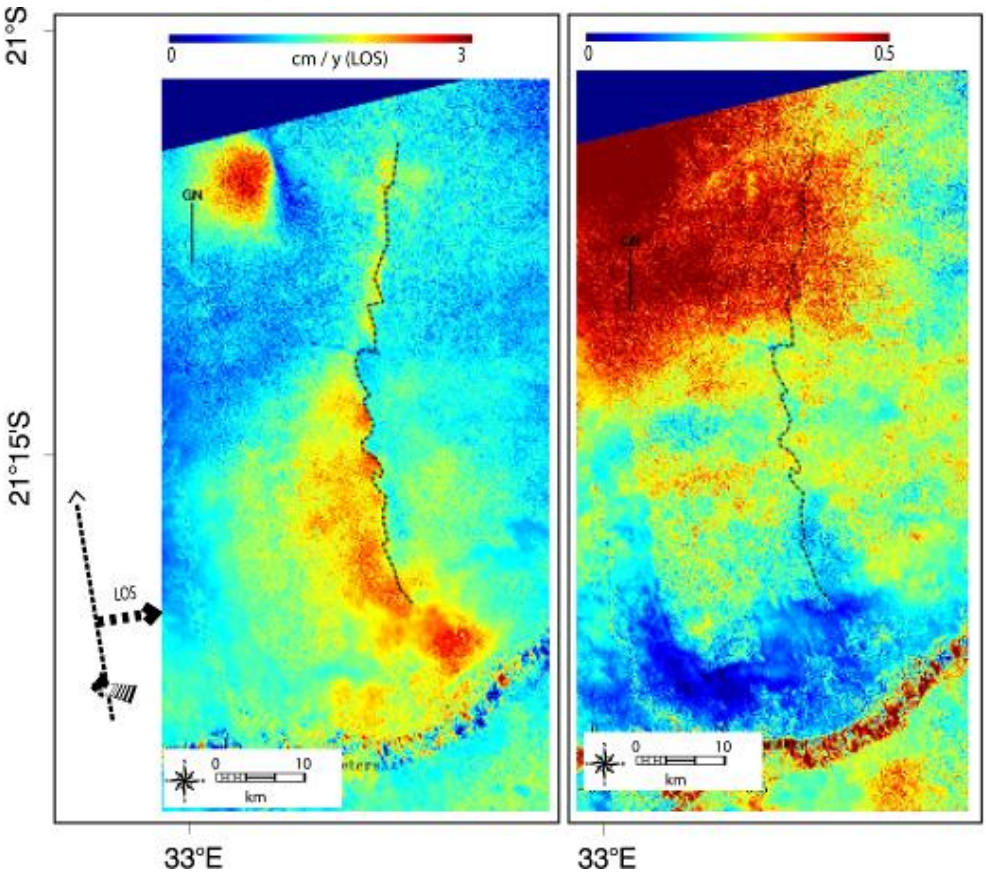

Figure 2 a): Average deformation (2006-2008) in Line of sight (cm/year). The surface rupture (dashed line) has been digitised on the image. b): RMSE (rad) of the re-ordered phase screens with respect to linear deformation (root-mean-square residual to the estimated constant rate LOS displacement). No correlation with the rupture position is observable.

Pre-seismic Displacement

Figure 3 shows interferograms for the inter-seismic periods 1993-1995 and 1993-1996. No surface displacement phenomena are identified in the vicinity of the seismogenic fault prior to the earthquake. This observation leads us to rule out the presence of measurable pre-seismic slip or creep on this segment of the fault.

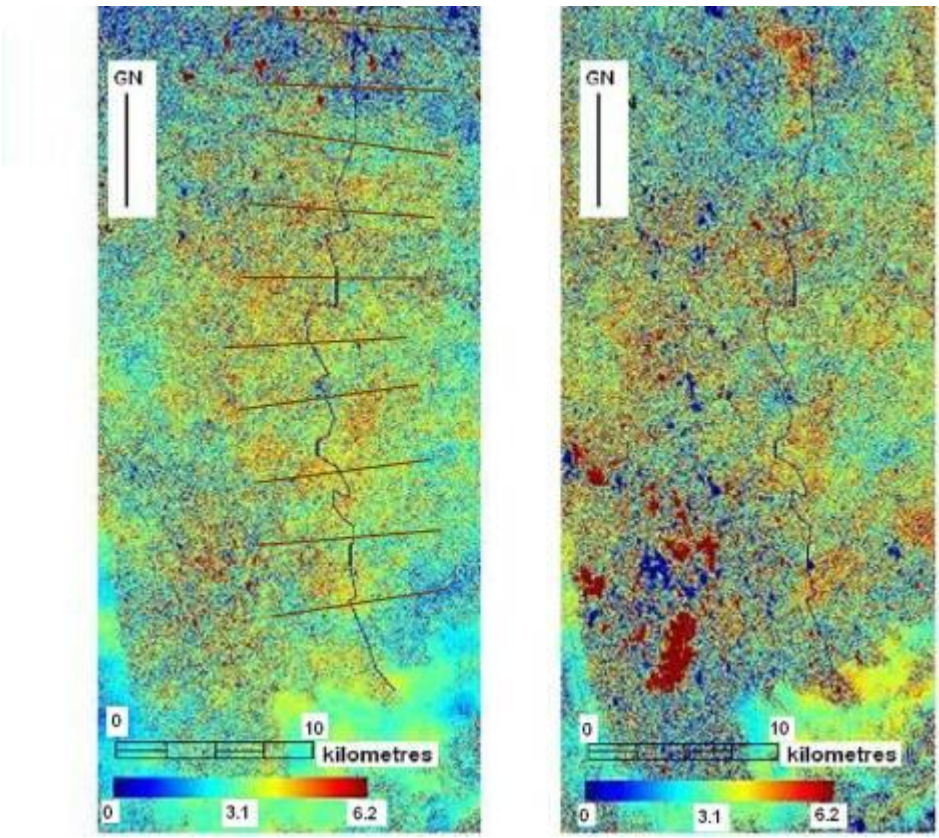

Figure 3: a) 1993-1995 JERS-1 interferogram. Black line: the seismogenic fault trace derived from the post-seismic displacement map. b) 1993-1996 JERS-1 interferogram. Values are given in radians. Positions of the ten 10-km profiles used for offset computation (Table 4) have been plotted.

In order to confirm the observation, using a profile tool from the cosi-corr software (Leprince and Ayoub, 2007) designed to estimate deformation-value differences on either side of a fault by comparing linear regressions, we derived the phase values. Table 4 presents the averages of estimations on ten profiles (from north to south) perpendicular to the fault location.

Table 4: offset (in rad) on either side of the fault estimated from the interferograms for ten profiles. Sigma corresponds to the standard deviations on the linear regressions on either side of the digitised fault computed by Cosi-corr.

Interferogram 1993-1995		***Interferogram 1993-1996***	
Offset (rad)	Sigma (rad)	Offset (rad)	Sigma (rad)
0.053	0.072	0.100	0.149

From Table 4 we can conclude:

- For the period 1993-1995, the mean deformation value equals approximately 0.05 rad (*i.e.* 0.09 cm), with a mean sigma of 0.07 rad (*i.e.* 0.12 cm)
- For the period 1993-1996, the mean deformation value equals 0.10 rad (*i.e* 0.2 cm), with a mean sigma of 0.15 (*i.e.* 0.3 cm)

The values obtained (about 1-3 mm) are very small in terms of the method sensitivity. There is accordingly no pre-seismic motion on the fault that is high enough to be observed with conventional INSAR.

Co-Seismic Deformation

Interferogram 2004/04/06 – 2006/05/07 (Figure 4) was selected as the most relevant for interpretation in terms of deformation. This interferogram provides information on the far-field deformation except on the northern area where the coherence is poor (probably because of vegetation). We will note that the deformation phenomenon observed in the post-seismic deformation map is located in the incoherent area. We thus cannot confirm, based on this interferogram, that a rupture did indeed occur at this location.

The near-field deformation is, of course, not measurable because the deformation gradients (metres of displacement on short distances) are far beyond what InSAR is capable of measuring.

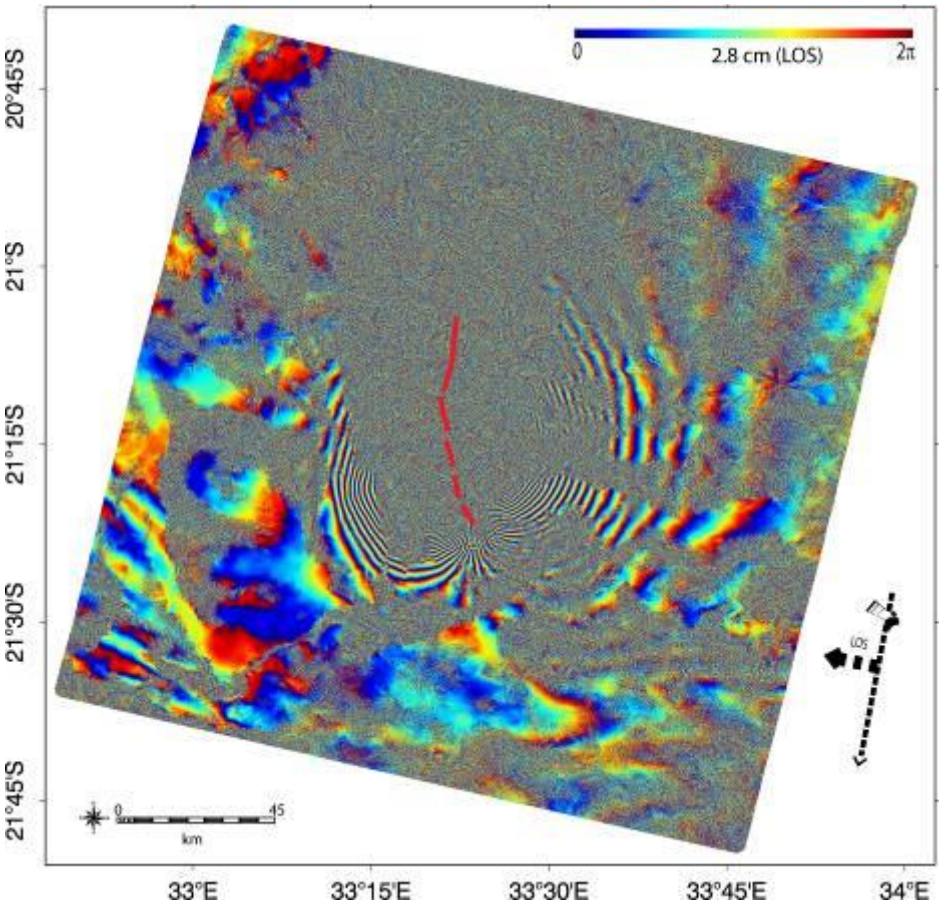

Figure 4 geocoded interferogram 2004/04/06 – 2006/05/07. One fringe corresponds to 2.8 cm of displacement in Line of sight. The position of the fault trace at the surface estimated from post-seismic deformation is shown.

Although the precision of image correlation applied to the radar amplitude images (with a slant range resolution of about 7 m) is much poorer than with interferometry, we tested the methodology in order to obtain an estimate of the deformation profile along the fault trace. This information could complement the radar interferometry information where surface displacement is too high (i.e. close to the rupture). Figures 5 and 6 show the results (offset image and deformation profile) of the correlation. The displacement values on the rupture are determined from linear least square fit to displacement profiles drawn perpendicularly to the rupture. Based on the a priori knowledge of the fault position, this procedure (Avouac et al., 2006; Leprince et al., 2007) fits the deformation profile perpendicularly to the fault by 2 half strait lines on either side of the fault (the profiles are limited by the same point on the fault); the deformation estimate is then provided by the difference between the two fitted values at the fault point location.

248 The observed displacement ranges from 1.5 to 2 m (consistent with Fenton & Bommer (2006) if we assume
249 that in view of the geometries of the fault (dip >70°) and the sensor (incidence ~ 2, we are mainly
250 measuring vertical deformation) in the southern part of the rupture and 0.7 m to 1.3 in the northern section
251 (consistent with Hasimoto et al. (2007) who proposed a smaller displacement on the northern segment).
252 Azimuth offsets were not used as they are not relevant to our study. Because the deformation is mainly
253 oriented east-west, there are no measurable offsets in the azimuth direction (~ south-north displacements)
254 taking into account the sensitivity of this technique if applied on ENVISAT ASAR data ($1/10^{th}$ of the pixel
255 size, i.e. ~ 40 cm).
256

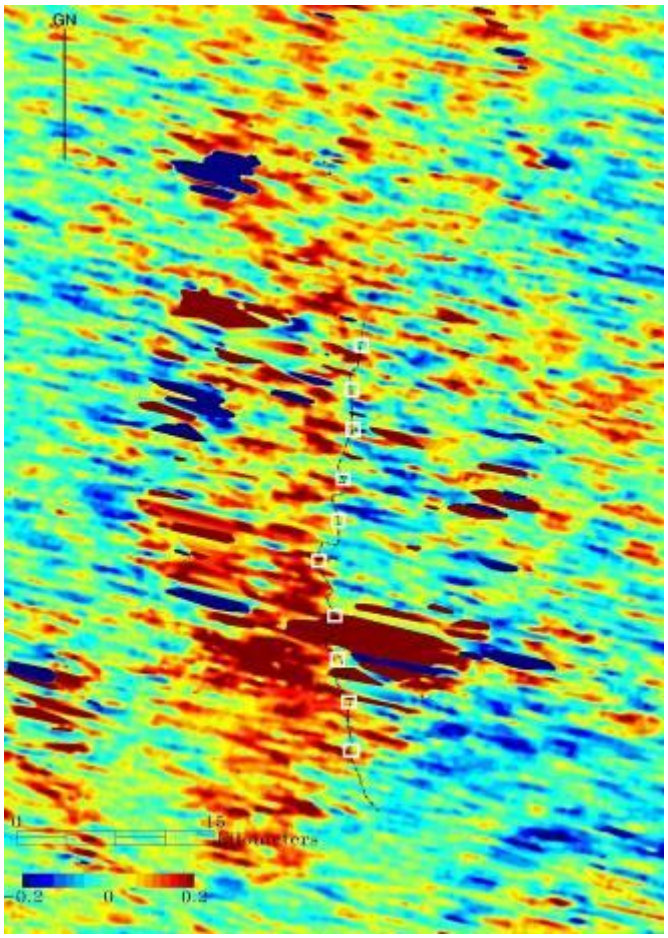

Figure 5: Slant range offset (in pixels of about 7 m) between images 2004/04/06 and 2006/05/07. The location of the rupture trace is shown. Squares indicate the location of the points on Figure 6, where offsets have been estimated. Although the result is noisy, the position of the rupture is consistent with the derived displacement variation.

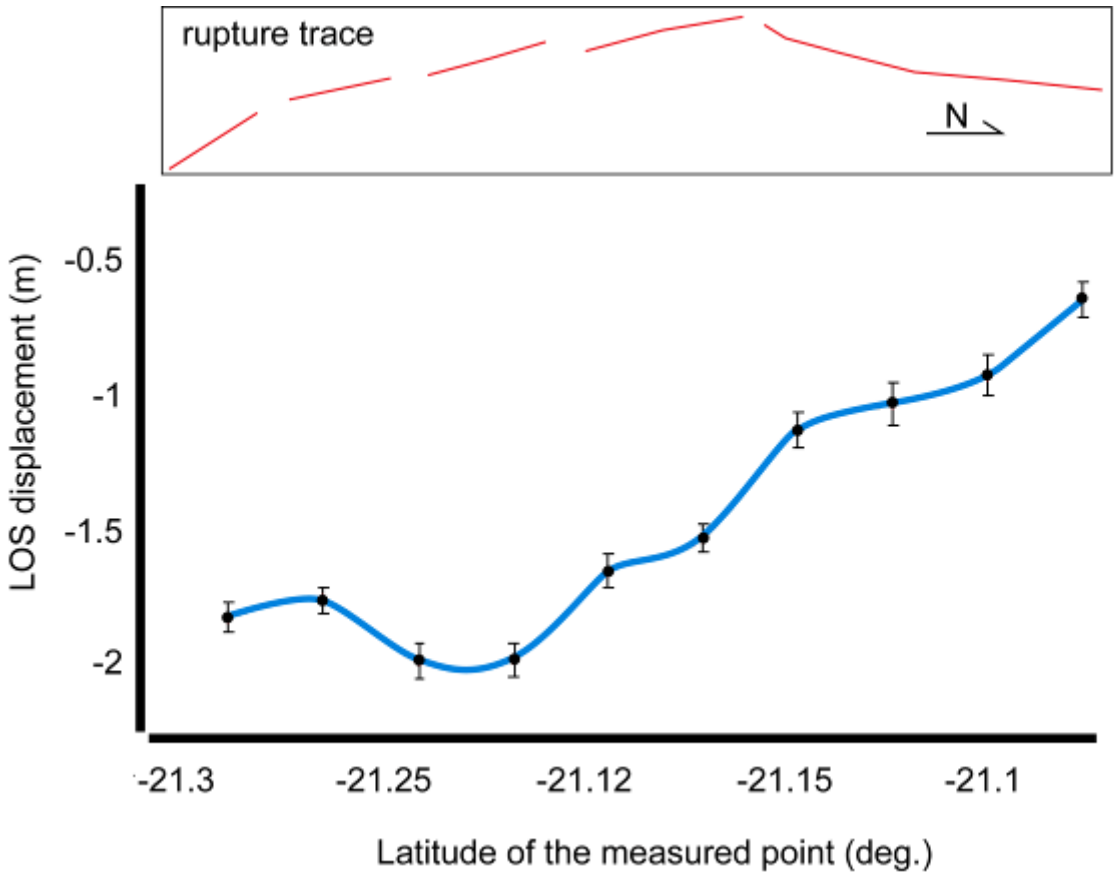

Figure 6: LOS displacement on the fault (in metres, east side with respect to west side) versus latitude obtained using the cosi-corr (Leprince and Ayoub, 2007) profile/stacking tool. The error bars correspond to the standard deviation in the linear regressions to either side of the fault.

5 Co-seismic deformation modelling

We propose an inversion based on an elastic dislocation model (Okada, 1985; Briole, 1986). Because of the large number of parameters (location, dip, depth, size, displacement for the two fault segments) to be inverted using only one component (Line of sight) of the deformation, we had to use pre-existing information (estimates of the parameters from Feitio, 2008) and trial-and-error adjustments to correct several of the parameters before inverting the slip values. For convenience, we used rake values of -90° for both segments (Feitio, 2008, used -80°).

As in Hasimoto et al., (2007) we propose a model with two contiguous fault segments implied in the deformation. However, the position and orientation of the segments are derived from the trace obtained from

283 the post-seismic deformation. Thus, the orientation of the northern segment differs from that proposed by
284 Hasimoto et al., (2007).
285 Table 5 summarizes the resulting parameters. The slip values are consistent with Hasimoto et al., (2007).
286
287 Table 5: Inverted model parameters.
288

Parameter	***Southern segment***	***Northern segment***
UTM 36 S east (km) of the centre of the segment	537	537
UTM 36 S north (km) of the centre of the segment	7647	7667
Segment azimuth (deg)	170	-172
Depth of the top of the segment (km)	5	3
Half length of the segment (km)	10	10
Width of the segment (km)	11	9
Dip (deg)	70	70
Slip (mm)	3400	2660

289

290 As described in section 3, the model obtained is suitable for inclusion in a procedure for improving the
291 unwrapping process and interpolating where the interferogram's coherence is inadequate. Figure 7 shows
292 the modified interferogram. We should state that improvement can be expected to be better in the far-field
293 deformation areas (where the model is more reliable, being derived from interferometric data unavailable in
294 the rupture zone). Near the rupture, the result still appears underestimated. For instance, the maximum
295 relative deformation is about 115 cm in LOS (i.e., about 125 cm in vertical) as opposed to 2 m observed by
296 Fenton & Bommer (2006) and Figure 7. However, the underestimation is much less than with a direct
297 unwrapping of the interferogram. We think that such interferogram unwrapping (once the area along the
298 rupture has been masked) could be used for inverting a more complex deformation model provided it was
299 combined with additional data. As only one component of deformation is available, if we intend to consider
300 inhomogeneous slips on the fault planes, we would need additional information in order to cope with the
301 non-uniqueness of the solution, in particular other components of deformation and a better description of

fault geometry. In fact, in the case of our simple model based on constant slip on two large surfaces combined with basic assumptions on the geometry, we do not believe that re-using these results to improve the model could provide better results than those based on data derived from displacement data obtained by fringe digitizing. To test such a possible “iterative” method (improve the previous model using the corrected interferograms), at least two components of deformation would be required. In the present test case, the available data set does not allow us to go further. Let us note that an additional advantage for such interferogram improvement would be to facilitate interferogram stacking. Indeed, if we had several interferograms for the same event, we would plan to average them in order to reduce noise or atmosphere or compensate for residual biases (not fully compensated). For such stacking procedures, prior unwrapping is needed. Because of the limitations of standard unwrapping with a high deformation gradient and areas of low coherence, such stacking could fail. In this perspective, the described procedure could prove helpful, but unfortunately in our test case only one reliable interferogram was actually produced.

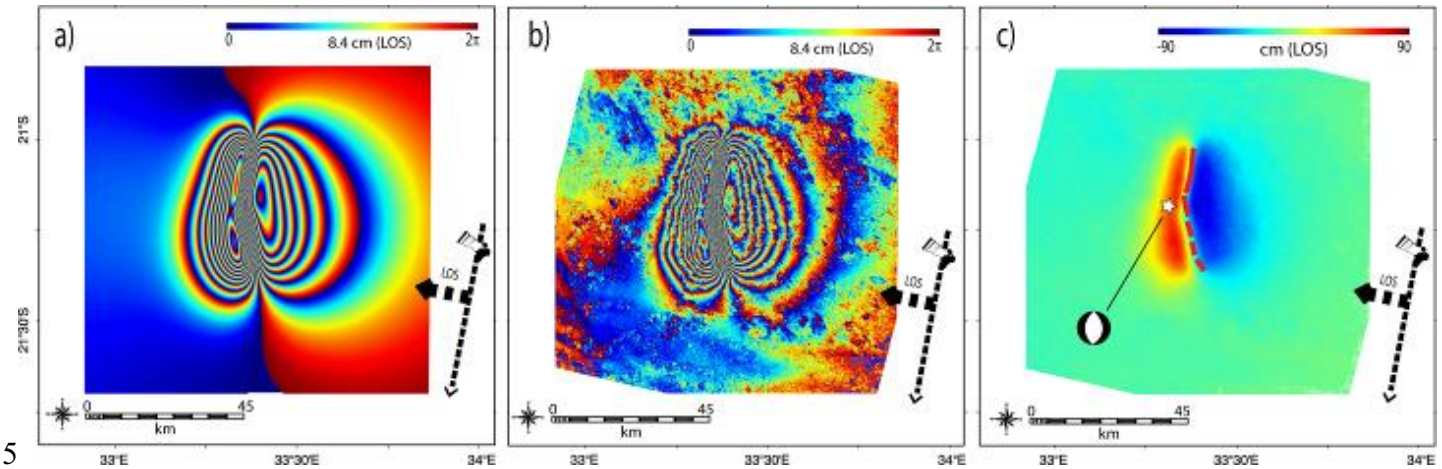

Figure 7: a) Interferogram simulation obtained using the inverted parameters. One fringe corresponds to 8.4 cm in LOS. The approximate locations of the modelled fault surfaces are shown. b) Interferogram 2004/04/06 – 2006/05/07 unwrapped taking into account the simulation and rewrapped for visualisation purposes (one fringe corresponds to 8.4 cm in LOS) c) Interferogram 2004/04/06 – 2006/05/07 geocoded and unwrapped taking into account the simulation. Values in rad. The fault trace derived from post-seismic deformation is shown.

8 Discussion and Conclusion

325 The results presented in this paper provide new information for understanding surface displacement of the
326 Machaze earthquake in a broad sense.
327 We have used Satellite-based Radar Interferometry to map surface displacement during three phases (inter,
328 co and post-seismic) of the seismic cycle associated with the 2006 Machaze earthquake. The area affected
329 by the Machaze earthquake is not instrumented on the ground and it is only partially accessible in the field
330 due to the presence of land mines. This makes satellite remote sensing techniques the only tools available
331 to make broad-scale measurements in the area allowing the whole earthquake-induced surface
332 displacement to be observed. We have made use of archive data from both L-band and C-band sensors on
333 board J-ERS, ALOS-PALSAR and ENVISAT-ASAR respectively. The use of J-ERS data drawn from
334 archives to try to enhance possible inter-seismic surface displacements is an interesting aspect of the InSAR
335 technique for such *a posteriori* studies.
336 As the surface displacement characteristics during the three phases of the seismic cycle differ in terms of
337 linearity, deformations gradients and localization, we adapted *ad hoc* processing strategies to the data
338 appertaining to each observation period. In particular, our study started by identifying the location of a
339 candidate surface rupture based on the post-seismic surface displacement location, which completes and
340 complements the surface rupture field observations made by Fenton & Bommer (2006). Interferogram
341 stacking (by averaging) was needed for inter- and post-seismic regimes, while for the co-seismic phase we
342 proceeded by visual selection of reliable interferograms from an extensive interferogram series and used a
343 simulation (from an elastic dislocation model) for improving phase unwrapping. Finally, we proposed a new
344 inversion of the earthquake parameters taking into account the identified rupture location.
345 The post-seismic deformation seems to be constant with time, about 3.5 cm/year for at least the two years
346 after the earthquake. Such a post-seismic phenomenon is intriguing and begs further dedicated
347 investigation. As far as this study is concerned, we tried to discriminate broadly among different possible
348 known source phenomena such as viscoelastic relaxation (e.g. Thatcher, 1983; Freed et al., 2007),
349 poroelastic rebound (e.g. Jonsson et al., 2003), afterslip (e.g. Marone et al., 1991) and dilatancy recovery
350 (e.g. Fielding et al., 2009). Although these phenomena might have occurred, we could reasonably rule out
351 substantial contribution from viscoelastic relaxation and poroelastic rebound, as these phenomena would
352 yield a post-seismic signal opposite in direction to the co-seismic signal, which was not the case here. The
353 dilatancy recovery phenomenon was observed geodetically on the BAM strike-slip fault system in Iran
354 (Fielding et al., 2009). Although this phenomenon in not well understood for normal faulting and certainly

would deserve more attention for the Machaze case, we might argue that dilatancy recovery would affect a broad zone in the fault area, one not particularly limited by the fault plane, which is not our case. Afterslip occurs when coseismic stress changes drive best candidate in the Machaze area, as its direction the same as that of the coseismic slip, a fact observed elsewhere (e.g. Freed, 2007).

In further work, we intend to address the following issues about this earthquake that deserve investigation. The post-seismic deformation over a longer period has to be monitored with the objective of detecting deformation slowing (or termination) in order to be able to model for this evolution.
Finally, the deformation observed north-north-west of the epicentre after the earthquake is still unexplained and should be investigated.

9 Acknowledgements

The study was conducted with the support of the Research Division of BRGM. Parts of the presented study were carried out in the framework of the MSc work of B. Ristori presented at Ecole Sup. des Géomètres et Topographes in June 2009. We wish to thank the reviewers for their help in improving the manuscript.

10 References

Avouac, J.P., Ayoub, F., Leprince, S., Konca, O., & Helmberger, D.V. (2006), The 2005, Mw 7.6 Kashimir earthquake: Sub-pixel correlation of ASTER images and seismic waveforms analysis, *EPSL*, 249, 514-528.

Briole, P., De Natale, G., Gaulon, R., Pingue, F., & Scarpa, R. (1986), Inversion of geodetic data and seismicity associated with the Friuli earthquake sequence (1976-1977) Italy, *Annales Geophysicae*, *4 B*, 481-492

Feitio P. (2008), Relocation of the Machaze and Lacerda earthquakes in Mozambique and the rupture process of the 2006 M_w 7.0 Machaze earthquake, Master Paper, IISEE, Tsubuka, Japon, (http://iisee.kenken.go.jp)

385 Fenton C. & Bommer J., (2006), The M_w 7 Machaze, Mozambique, Earthquake of 23 February 2006,
386 *Seismological Research Letters, 77*, 426-432
387
388 Fielding, E.J., Lundgren, P.R., Bürgmann, R., Funning, G.J., (2009), Shallow fault-zone dilatancy recovery
389 after the 2003 Bam earthquake in Iran, *Nature, 458*, 64-68
390
391 Freed, A.M., (2007), Afterslip (and only afterslip) following the 2004 Parkfield, California, earthquake,
392 *Geophysical Research Letters*, *34*, art. no. L06312
393
394 Gamma RS, (2008), "IPTA Reference Manual", Gamma RS, Gumligen
395
396 Hashimoto M., Fukushima Y. & Ozawa T. (2007), co-seismic and post-seismic displacements from the
397 Mozambique earthquake of 22 February 2006 detected by InSAR, *Fringe07*, Frascati, Italy, 26th-30th
398 November 2007
399
400 Jónsson, S., Segall, P., Pedersen, R., Björnsson, G., (2003), *Post-earthquake ground movements correlated*
401 *to pore-pressure transients,* Nature, 424 (6945), 179-183
402
403 Le Mouélic S., Raucoules D., Carnec C.& King C., (2005), A Least-squares adjustment of multi-temporal
404 InSAR data – Application to the ground deformation of Paris*, Photogrammetric Engineering and Remote*
405 *Sensing*, *2*, 197-204
406
407 Leprince S. & Ayoub F., (2007),Cor-registration of Optically Sensed Images and Correlation. *User's Guide to*
408 *COSI-CORR,* California Institute of Technology, Pasadena
409
410 Leprince S., Ayoub F., Klinger Y. & Avouac J.P., (2007), Co-Registration of Optically Sensed Images and
411 Correlation (COSI-Corr): an Operational Methodology for Ground Deformation Measurements, IGARSS
412 2007, 23-27 July 2007 - Barcelona, Spain

López-Querol, S., M. Coop, W.W. Sim, J.J. Bommer & C. Fenton, (2007), Back-analysis of liquefaction in the 2006 Mozambique earthquake. Georisk 1(2), 89-101.

Marone, C.J., Scholtz, C.H., Bilham, R., (1991), On the mechanics of earthquake afterslip, *Journal of Geophysical Research, 96* (B5), 8441-8452

Massonnet, D. & Feigl, K.L., (1998), Radar interferometry and its application to changes in the earth's surface, *Reviews of Geophysics, 4*, 441-500.

Michel R. & Avouac J., (2002), Deformation due to the 17 August 1999 Izmit, Turkey, earthquake measured from SPOT images. *Journal of Geophysical Research B: Solid Earth, 4*, 2-1.

Okada, Y.,(1985), Surface deformation due to shear and tensile faults in a Halfspace, *Bull. Seismol. Soc. Amer.*, *75*, 1135–1154

Raucoules D., Colesanti C. & Carnec C., (2007), Use of SAR interferometry for detecting and assessing ground subsidence, *Compte Rendus Geosciences*, *5*, 289-302

Thatcher, W., (1983), Nonlinear strain buildup and the earthquake cycle on the San Andreas fault. *Journal of Geophysical Research, 88* (B7), 5893-5902

Wegmuller, U., Werner, C. & Strozzi, T., (1998), SAR interferometric and differential interferometric processing chain. *International Geoscience and Remote Sensing Symposium (IGARSS), 2*, 1106-1108, July 1998, Seattle

Figure 1

Click here to download high resolution image

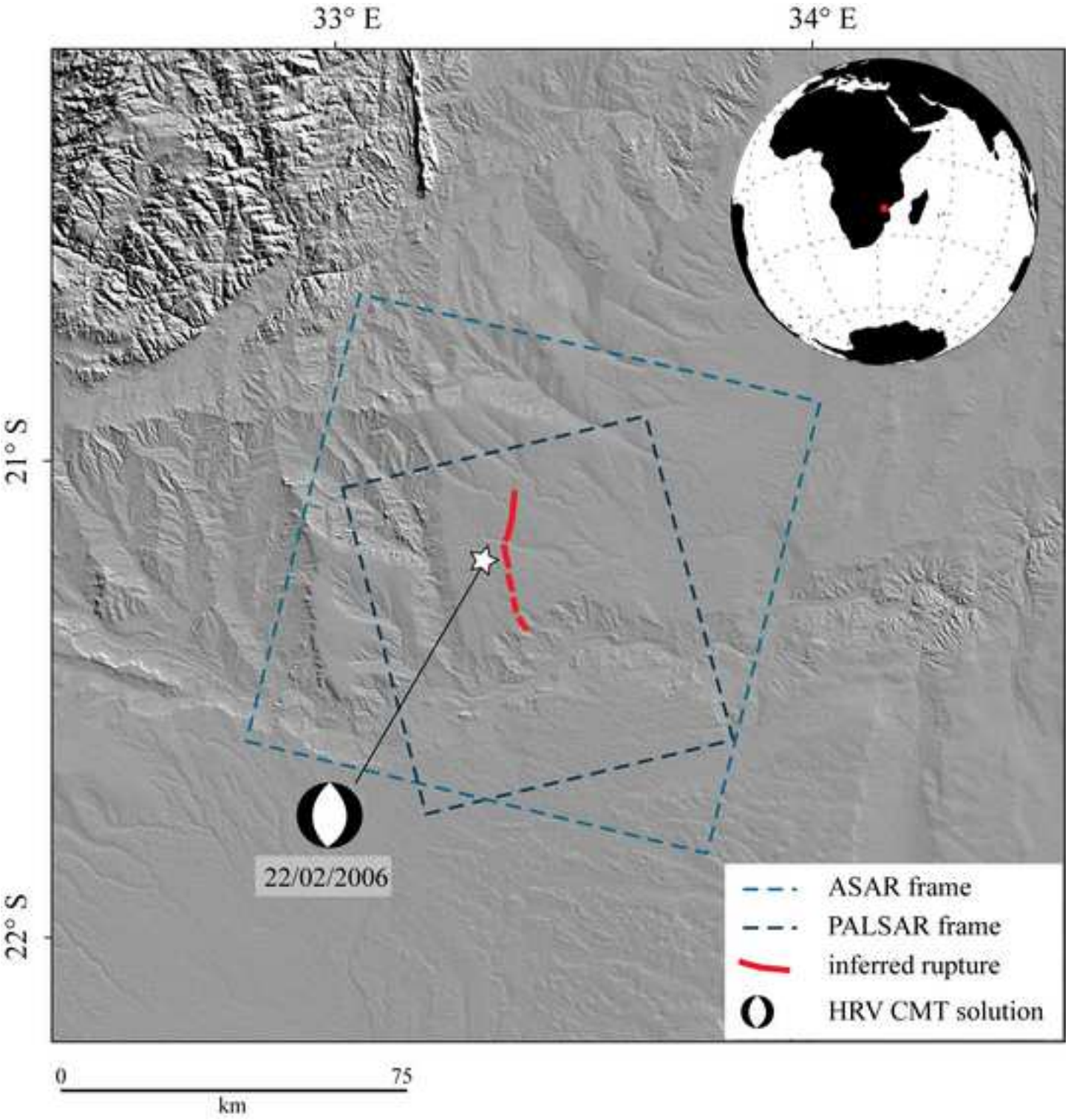

Figure 2

Click here to download high resolution image

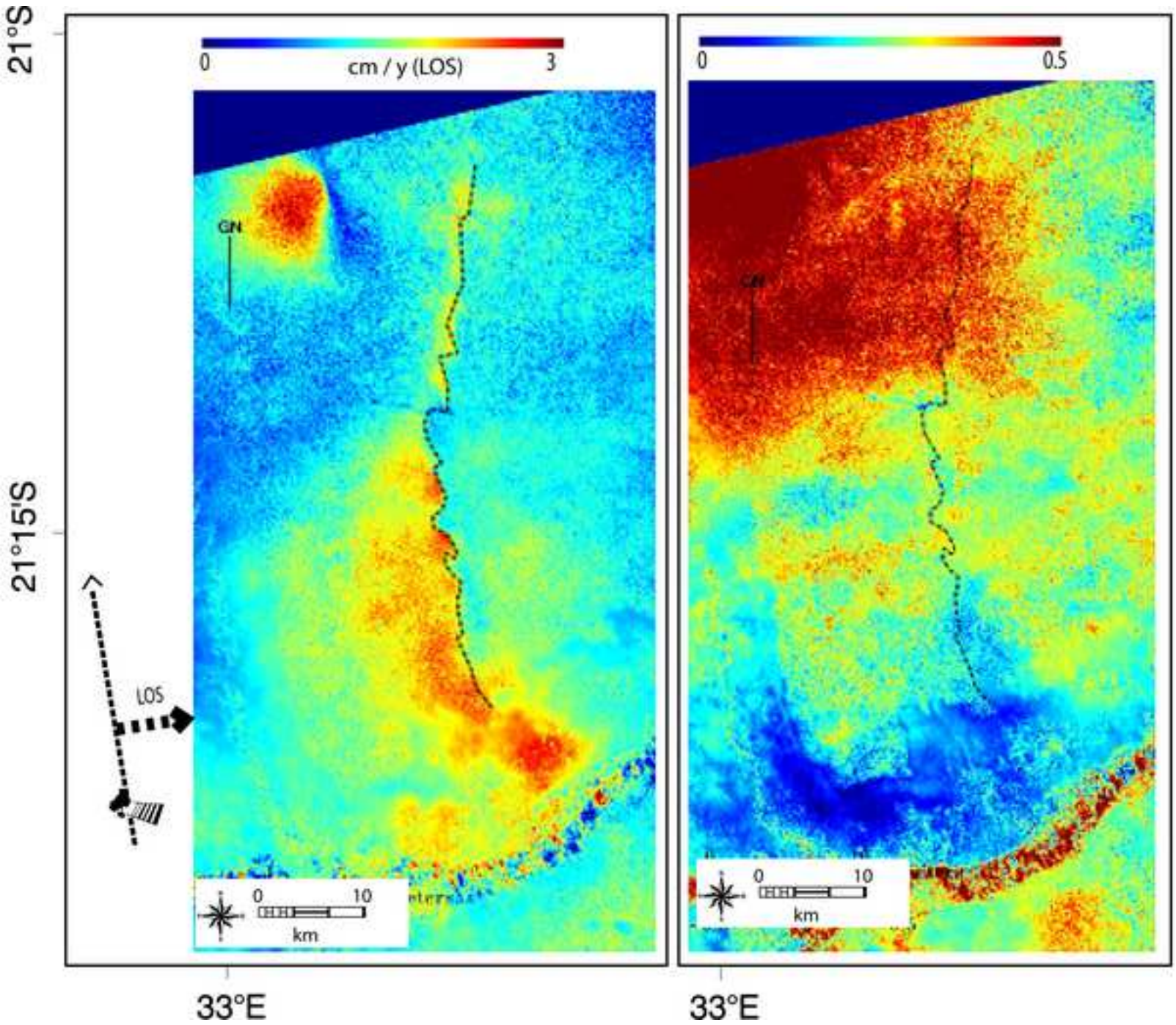

Figure 3

Click here to download high resolution image

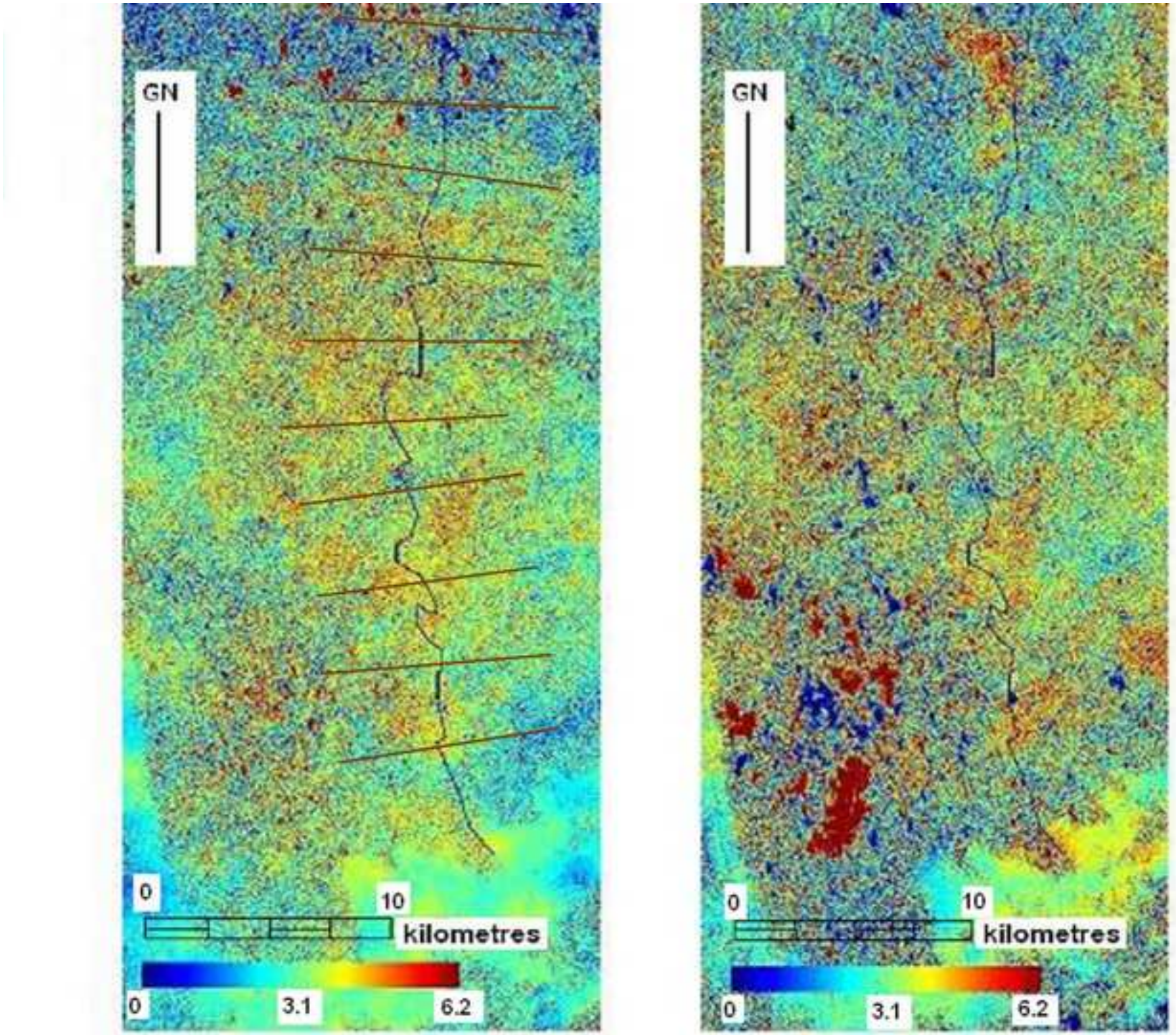

Figure 4

Click here to download high resolution image

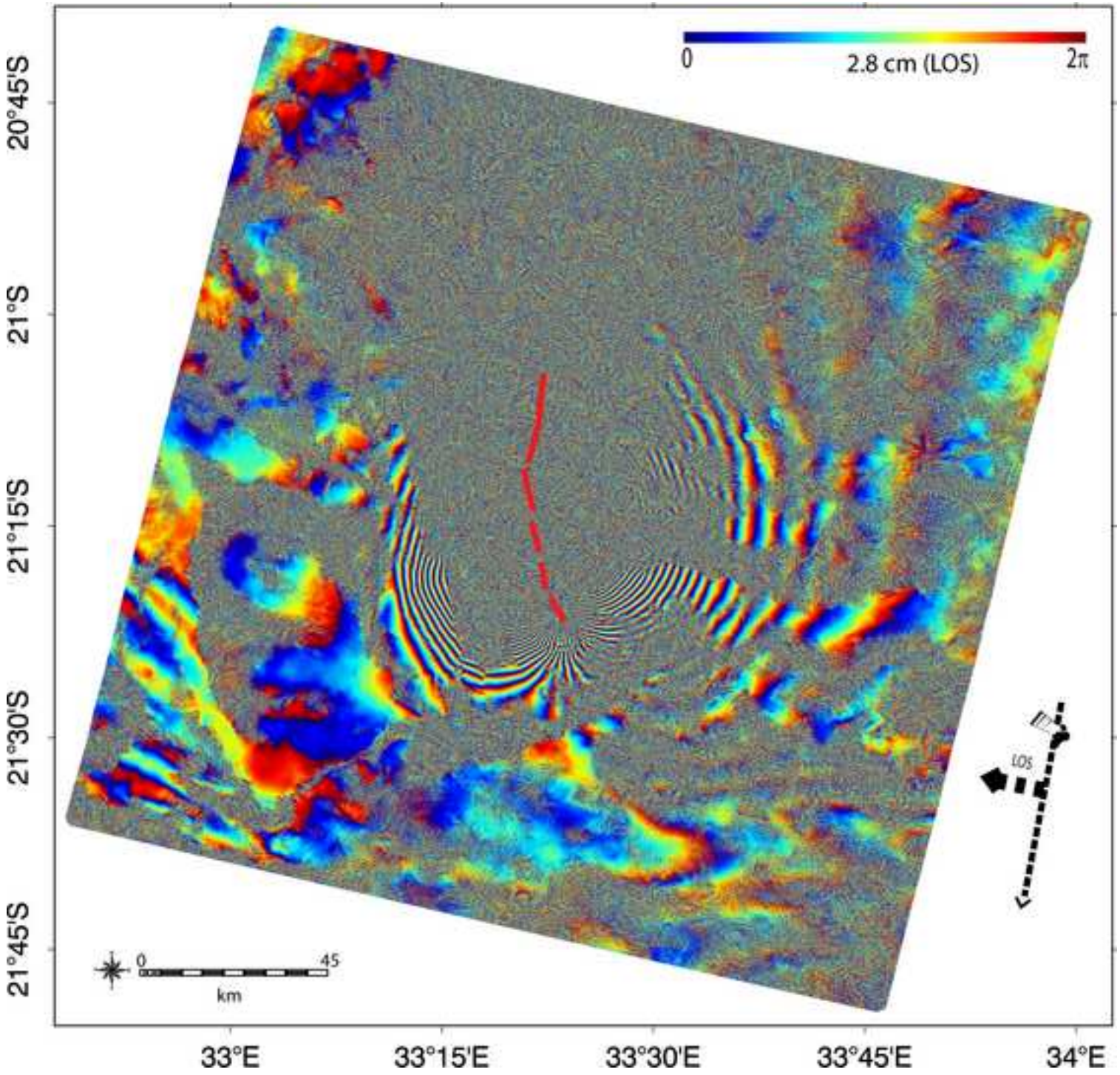

Figure 5

Click here to download high resolution image

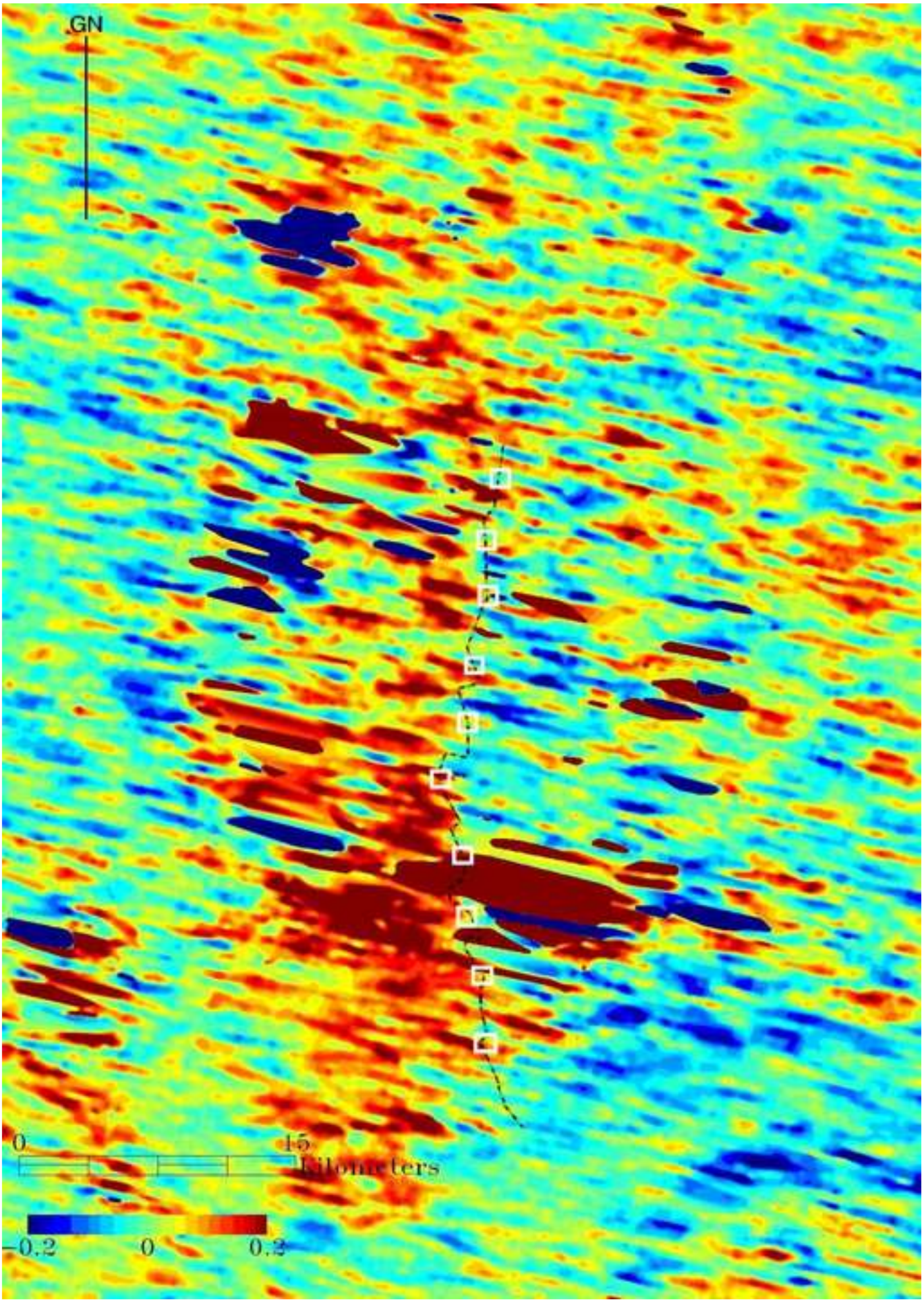

Figure 6

Click here to download high resolution image

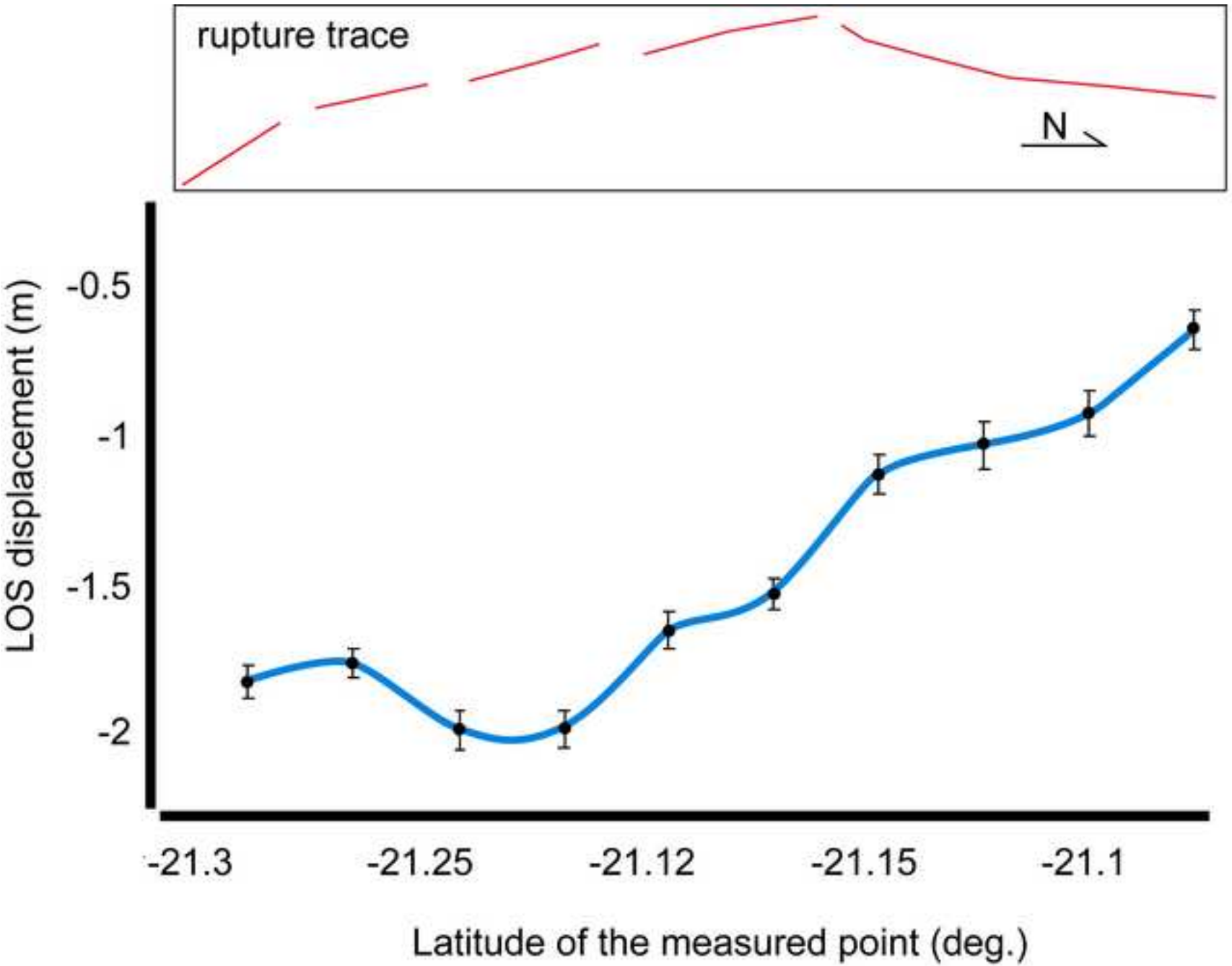

Figure 7

Click here to download high resolution image